Successive bifurcations in directional viscous fingering

H. Z. Cummins,* L. Fourtune, and M. Rabaud

Laboratoire de Physique Statistique, Ecole Normale Supérieure, 24 rue Lhomond, 75231 Paris CEDEX 05, France

Directional viscous-fingering experiments are reported which extend previous studies by Rabaud, Michalland, and Couder [Phys. Rev. Lett. **64**, 184 (1990)]. With the external cylinder rotation speed V_e fixed at a small constant value, the counter-rotation speed of the inner cylinder V_i, which is then the single control parameter of the experiment, was increased or decreased in small steps. Beyond the primary planar-cellular bifurcation of the air-oil interface, a secondary bifurcation was observed to a state with uniform space-filling traveling cells, followed by a spatial period-doubling bifurcation. Close to these bifurcations, we also observed transient states with solitary traveling cells, traveling domains of tilted cells, and mixed states of coexisting large and small traveling cells. These states resemble observations in recent directional-solidification experiments on liquid crystals and eutectic alloys. We discuss these results in the context of recent theoretical descriptions of parity-breaking tilt bifurcations and spatial period-doubling bifurcations based on k-$2k$ mode-interaction models.

PACS number(s): 47.20.Ky, 47.20.Hw, 68.10.−m

I. INTRODUCTION

Pattern-forming instabilities of quasi-one-dimensional fronts exhibit a rich variety of dynamical behavior and have been studied extensively in recent years. The well-known Mullins-Sekerka free-solidification instability and the Saffman-Taylor instability, which both involve the experimental complication of uncontrolled movement of the front, each have an analog in which the front is conveniently localized in the laboratory frame of reference: directional solidification and directional viscous fingering (DVF), respectively. In directional solidification, the position of the front is constrained by a temperature gradient, while in DVF, a gradient in the thickness of the fluid layer provides the constraint. For both, the stabilizing gradient also shifts the wave vector of the initial instability from $k = 0$ to a nonzero value.

DVF (also called the printer's instability) has been studied [1–7] with the apparatus illustrated schematically in Fig. 1 in which a small amount of oil is placed between two glass cylinders separated at the bottom by a small adjustable gap of thickness b_0. (A review of earlier investigations of various coating-flow instabilities, including DVF, can be found in Refs. [6] and [8].)

Previous experiments with this apparatus have identified several dynamical regimes exhibiting stationary cells, traveling cells, solitary waves, and spatiotemporal chaos as indicated in the state diagram of Fig. 2 (from Ref. [3]). In these experiments, it was found that if the rotational velocity of the inner (or outer) cylinder is increased with the other cylinder stationary, there is a critical rotation velocity V_c (which increases linearly with b_0) at which the planar oil-air interface undergoes a supercritical bifurcation to a stationary cellular pattern. Further increase of V causes the amplitude of the cells to increase while their wavelength decreases, but the cells remain stationary, and left-right symmetry is preserved at all accessible values of V. If the inner cylinder velocity is

set well above V_c and the outer cylinder is then set into counter-rotation (as indicated by the downward arrow A in Fig. 2), another bifurcation occurs immediately to a broken-parity traveling cell regime [4].

Following the discovery of a "tilt bifurcation" in directional solidification experiments of a nematic-isotropic liquid-crystal interface by Simon and co-workers [9,10], several theoretical analyses have appeared, mainly based
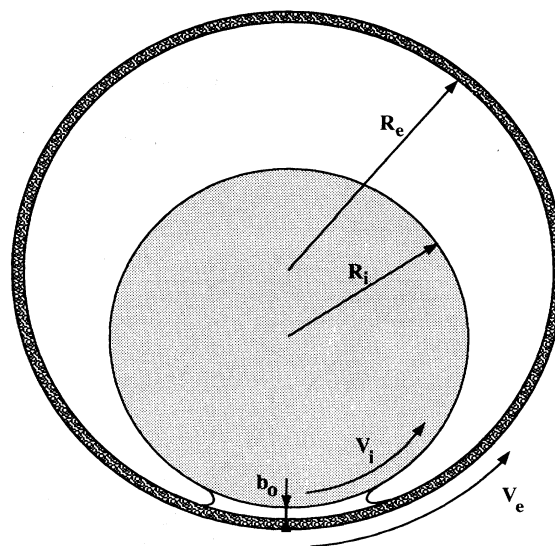

FIG. 1. Sketch of the DVF apparatus showing the two cylinders and the menisci. Inner glass cylinder is 38 cm long and of radius $R_i = 33$ mm (precision ±0.01 mm). The outer Pyrex cylinder is 42 cm long and of radius $R_e = 50$ mm (precision ±0.03 mm). The fluid used is Rhodorsil silicone oil 47V100 (dimethyl polysiloxane) $\rho = 0.965; \eta(25 \,°C) = 100$ mm^2/s. The width of the oil layer (viewed from below) is ∼5 cm.
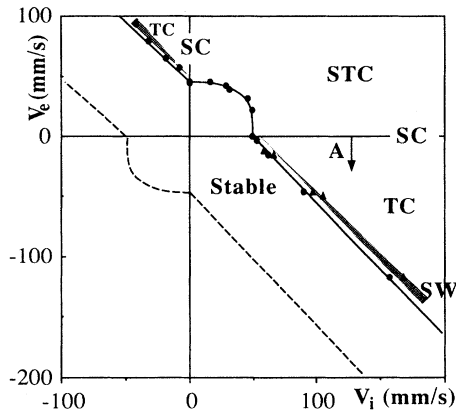
FIG. 2. State diagram of one interface in the (V_e, V_i) plane with $b_0 = 0.37$ mm. The observed dynamical regimes are labeled SC (stationary cells), TC (traveling cells), SW (solitary waves in gray), STC (spatiotemporal chaos) (from Ref. [4]).

on amplitude (or time-dependent Landau) equations, which predict that as the control parameter increases, a first bifurcation to a cellular state should appear, followed by a secondary "tilt bifurcation" to a broken-parity traveling cell state. Although this scenario does occur in directional solidification where domains of traveling cells or solitary propagating cells appear in transforming liquid crystals [9,10] or solidifying eutectic alloys [11–13] as the pulling speed is increased, it has not been thought to apply directly to DVF since increasing the primary control parameter V_i produces a planar-cellular bifurcation, but the tilt bifurcation does not occur as a steady state unless the second control parameter V_e is also increased to a nonzero value. (A tilt bifurcation may occur as a transient with $V_e = 0$, however, following a sudden increase in V_i [5].)
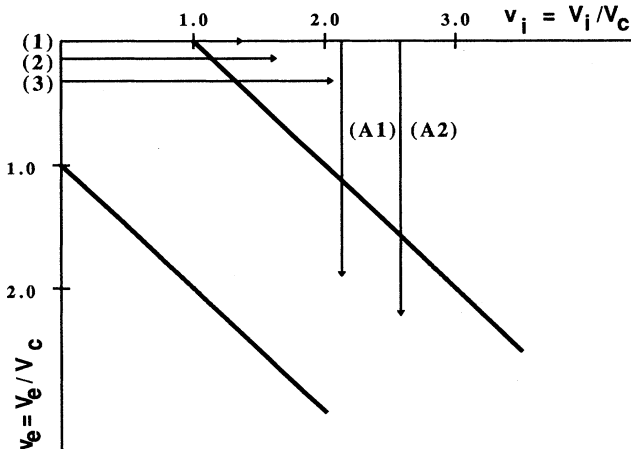

FIG. 3. Region of the state diagram explored in the present investigation. Horizontal trajectories: (1, $v_e = 0$), (2, $v_e = 0.1$), (3, $v_e = 0.25$). Vertical trajectories: ($A1$, $v_i = 2.1$), ($A2$, $v_i = 2.6$).

The main experiments described in this paper were performed somewhat differently than previous experiments in that the outer cylinder was first set into steady rotation at a selected speed V_e, well below V_c, and V_i was then gradually increased (or decreased) along one of the horizontal trajectories indicated by (2) or (3) in Fig. 3. In these experiments, with $V_e \geq 0.1 V_c$, successive planar-cellular, cellular-propagating, and spatial period-doubling bifurcations were found to occur.

We view the slow rotation of the outer cylinder in these experiments as fixing a boundary condition rather than as a second control parameter. The qualitative difference between trajectory (1) ($V_e = 0$) and the other horizontal trajectories (2), (3) ($V_e \neq 0$) is that rotation of the outer cylinder introduces a wetting layer so that the interface is confined between two wet boundaries, while then $V_e = 0$, the outer boundary is dry. This qualitative difference is the probable origin [14] of the "bifurcation at zero" observed in previous experiments following the downward vertical trajectory A of Fig. 2 [4].

II. EXPERIMENTS

Two series of experiments were performed with the apparatus shown schematically in Fig. 1, the first with $b_0 = 0.5$ mm, and the second principal series with $b_0 = 0.7$ mm. The (v_i, v_e) trajectories followed in these experiments are indicated in Fig. 3. Note that the velocities of the inner and outer cylinders V_i and V_e have been replaced by dimensionless velocities v_i and v_e, scaled to the planar-cellular bifurcation threshold velocity V_c for single-cylinder rotation ($V_c = 74$ mm/s for $b_0 = 0.5$ mm, $V_c = 115$ mm/s for $b_0 = 0.7$ mm). These primary bifurcation threshold values, and the secondary bifurcation threshold values as well, are somewhat sensitive to the oil level which changes with time because of a slow oil leak in the apparatus. Furthermore, minor imperfections in the cylinders and their alignment also cause small time-dependent changes in the interface profile which are particularly evident close to threshold. Consequently, the data trend to exhibit considerable scatter for values of v_i and v_e close to the bifurcation thresholds.

In the first set of experiments, the horizontal $v_e = 0$ trajectory (1) in Fig. 3 was explored initially, followed by several vertical trajectories ($A1, A2, \ldots$). In the second set of experiments, several horizontal trajectories (2),(3), $\ldots$ were studied with v_e fixed at $0.1, 0.25, \ldots$ respectively.

A. $v_e = 0$ trajectory (1)

Figure 4 shows a sequence of interface profiles obtained with the outer cylinder stationary, and the inner cylinder rotating with (dimensionless) speeds v_i between 1.0 and 3.33. As v_i increases, the wavelength λ decreases, while the peak-to-peak amplitude increases. The front, which is sinusoidal for velocities just above threshold, becomes increasingly distorted with increasing v_i and, at $v_i \sim 1.25$, becomes reentrant. For $v_i > 2.0$, the front resembles a series of Saffman-Taylor air fingers separated by oil walls which become progressively thinner as v_i in-
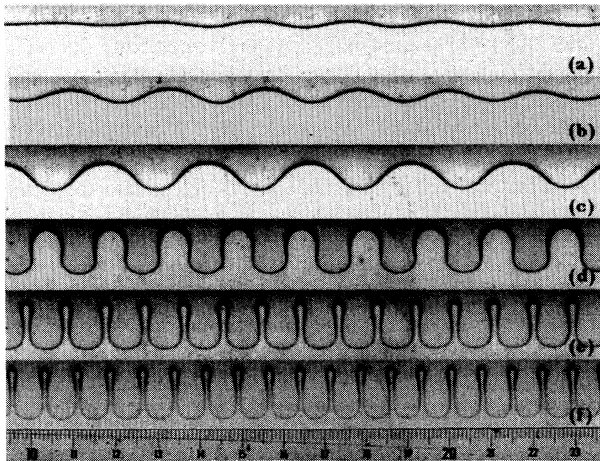
FIG. 4. Observed interface profiles for trajectory (1) ($v_e = 0$) for spacing $b_0 = 0.7$ mm, with (top to bottom) $v_i = 1.00$ (a), 1.02 (b), 1.07 (c), 1.28 (d), 2.32 (e), and 3.33 (f). In these images, the air is above the oil. The scale is in centimeters.

creases [2]. The evolution of the interface profile continues in this manner up to $v_i = 10.0$, the highest value studied in this experiment, with no evidence of an approaching second bifurcation. In a previous experiment, v_i was increased up to 50 with similar results [3].

Following a rapid increase of v_i, the pattern usually adjusts by tip splitting with some shifting of cells. Occasionally, we observe a transient domain of slowly drifting tilted cells which eventually dies out. In either case, the stationary patterns consist of regular symmetric vertical cells which do not move (stationary cells).

The domains of slowly drifting tilted cells do not create or destroy existing stationary cells but do modify their size [5]. They have recently been designated as "tilt domains" by Faivre and Mergy [11] and also closely resemble the "solitary modes" described by Simon, Bechhoefer, and Libchaber [9] and Flesselles, Simon, and Libchaber [10]. These tilt domains are dynamical defects which provide a wavelength-selection mechanism. Recent eutectic solidification experiments [11,12] have also revealed stable homogeneous space-filling tilted traveling cell states similar to those we will describe below.

Several series of charge-coupled-device video images similar to those shown in Fig. 4 were recorded with a Macintosh IIx computer. Preliminary analysis showed that the measured amplitudes and wavelengths were not reproducible for settling times less than ~30 min, especially close to threshold. The experiments discussed here therefore all allowed settling times of at least 30 min, and even longer near threshold. For each run, the printed images were measured to determine the wavelength and amplitude. As seen in Fig. 5(a), the peak-to-peak (p-p) amplitude increases rapidly with increasing v_i, essentially saturating near 12 mm. Also, as seen in Fig. 5(b), after a brief increase [15], the wavelength decreases rapidly at first, then more slowly, as observed in previous experiments [1].

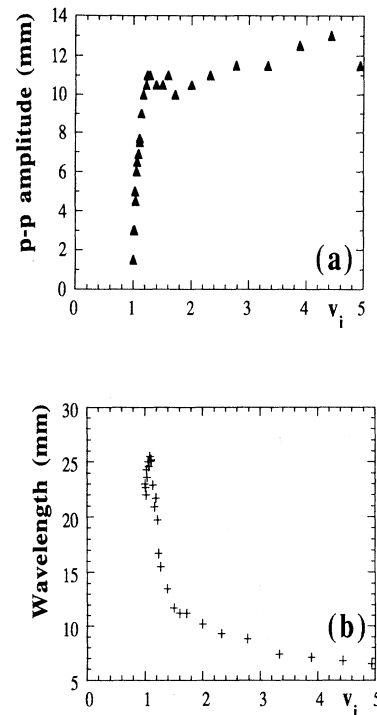Digitized interface profiles were Fourier analyzed with

FIG. 5. p-p amplitude (a) and wavelength (b) vs v_i on trajectory (1) ($v_e = 0$) for spacing $b_0 = 0.7$ mm.
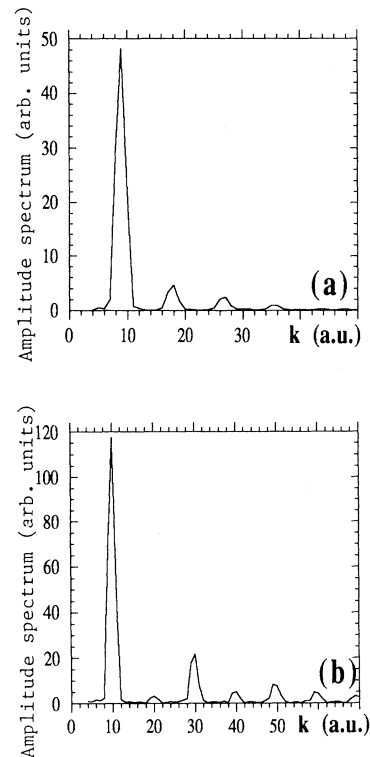

FIG. 6. Spatial FFT of interface profiles (for spacing $b_0 = 0.5$ mm) showing in arbitrary units the amplitudes (p-p) of the fundamental and first harmonics for $v_i = 1.05$ (a) and $v_i = 1.18$ (b) with $v_e = 0$. Note the dominance of the odd harmonics in (b).

a fast-Fourier-transform (FFT) computer program, and the amplitudes of the fundamental and first four Fourier harmonics were extracted to determine the harmonic content of each pattern. Two such Fourier spectra are shown in Fig. 6. Note the dominance of odd harmonics at $v_i = 1.18$. The values of A_n / A_1 for $n = 2$, 3, 4, and 5 at values of v_i up to 1.25 (where the patterns become reentrant) were plotted, and we found that while the content of odd harmonics (A_3 / A_1 and A_5 / A_1) increase with increasing v_i, the even harmonics (A_2 / A_1 and A_4 / A_1) decrease.

B. Vertical trajectories (A)

When v_i is set well above threshold and v_e is increased from zero in counterrotation [trajectories $A1$ ($v_i = 2.1$) or $A2$ ($v_i = 2.6$) in Fig. 3], propagating regions appear separated by transient locally chaotic regions. After about 10 min, the pattern becomes uniform, although often there are regions of coexisting left- and right-traveling cells separated by a source or sink which persists for long times. Within each domain one finds a regular array of cells within a constant drift speed v_d.

In each sequence of type A, v_i was set to a selected value, and v_e was increased in steps. After each step, the pattern was allowed to settle before being measured. Figure 7 shows a set of images for one such sequence with $v_i = 2.1$, $v_e = 0$, 0.05, 0.1, 0.19, 0.58, 0.77, and 0.96. At very small v_e (< 0.05), the cells tilt, breaking the left-right symmetry, and begin to travel with drift speed v_d, becoming progressively more asymmetric. Their drift

speed v_d increases with increasing v_e, reaches a maximum, and then decreases as the cell amplitude decreases. Eventually, the cells again become stationary, before disappearing as the trajectory approaches the boundary of the stable (planar) region in Fig. 2 and restabilizes ($v_e > 1$). In an extensive set of such experiments we found that at fixed v_i, in the region below the maximum in v_d, $v_d \sim (v_e)^{1/2}$.

C. Horizontal trajectories with $v_e \neq 0$

The principal set of experiments was performed with $b_0 = 0.7$ mm and the external velocity v_e fixed successively at $v_e = 0.10$, 0.18, 0.25, 0.35, 0.42, and 0.50. With v_e fixed, v_i was increased (or decreased) in small steps along one of the horizontal trajectories (2),(3), in Fig. 3. These experiments, which we will describe here in some detail, showed that for such horizontal trajectories the system exhibits three successive bifurcations with no observable hysteresis, at $v_i = v_{c1}$, v_{c2}, and v_{c3}, respectively.

Figure 8 shows a series of interface profiles for v_i values along the horizontal trajectory (2) of Fig. 3, with $v_e = 0.10$. The first three are beyond the primary planar-cellular bifurcation at v_{c1}, and exhibit stationary cells. The fourth, with $v_i = 1.39$, is just beyond the second (tilt) bifurcation at $v_i = v_{c2} \sim 1.38$, and consists of traveling small tilted cells (S cells) with drift speed $v_d = 3.1$ mm/sec and average wavelength $\lambda = 14.8$ mm.

As v_i is further increased, λ, which initially decreases smoothly with increasing v_i, suddenly *increases* near $v_i = v_{c3} = 1.52$, approximately doubling the cell size. This S-L bifurcation is characterized by the appearance of highly asymmetric rapidly moving large cells (L cells) seen in Fig. 8(f) at $v_i = 1.56$. (Note that in the vertical trajectory sequence $A1$) shown in Fig. 7, the S-L bifurca-
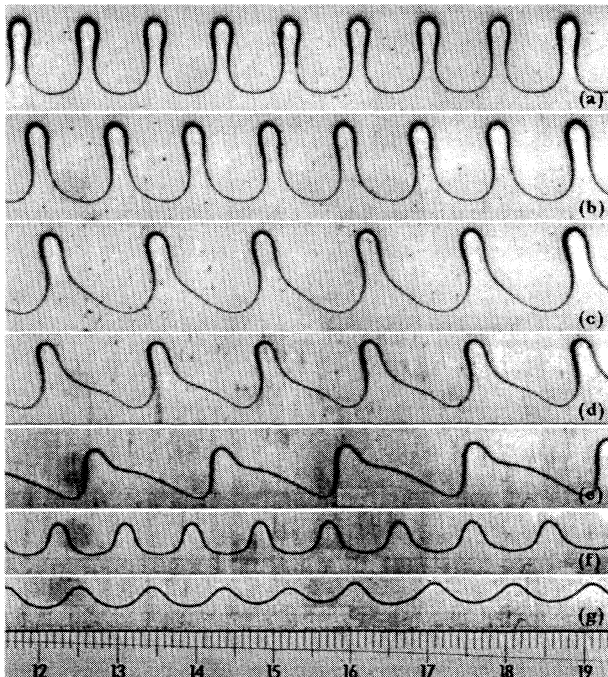

FIG. 7. Interface profiles for $v_i = 2.1$ (trajectory $A1$) with $v_e = 0$ (a), 0.05 (b), 0.1 (c), 0.19 (d), 0.58 (e), 0.77 (f), and 0.96 (g). Spacing is $b_0 = 0.5$ mm.
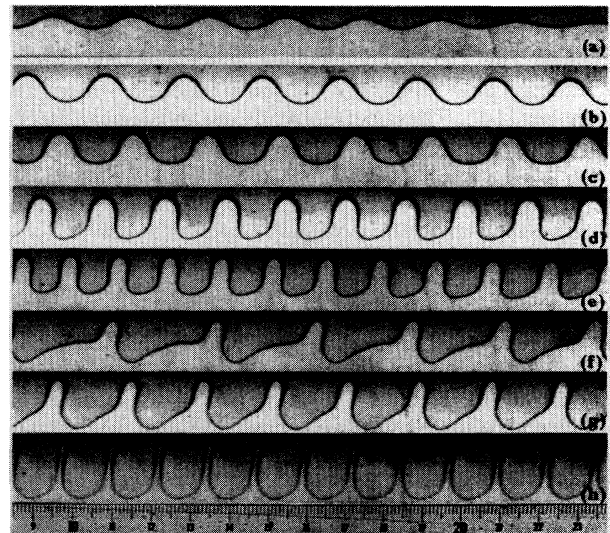

FIG. 8. Interface profiles for the horizontal trajectory (2) $v_e = 0.10$ and spacing $b_0 = 0.7$ mm, $v_i = 1.17$ (a), 1.26 (b), 1.33 (c), 1.39 (d), 1.50 (e), 1.56 (f), 1.94 (g), and 4.44 (h). The tilt bifurcation occurred near $v_i = v_{c2} = 1.38$, between (c) and (d). The S-L bifurcation occurred near $v_i = v_{c3} = 1.52$, between (e) and (f).
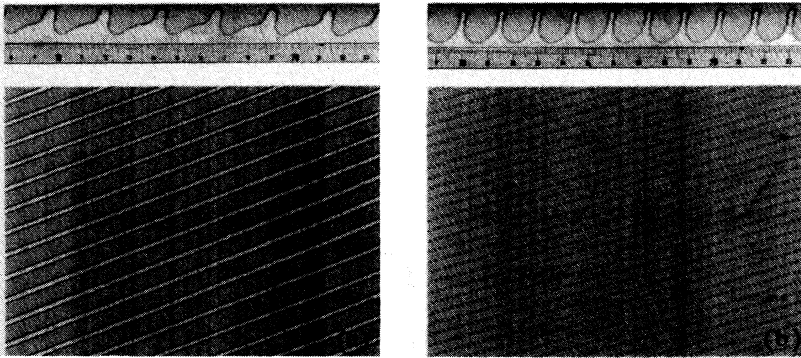
FIG. 9. Images (top) and single video-line spatiotemporal records (bottom) for (a) $v_e = 0.1$, $v_i = 1.61$, and (b) $v_e = 0.1$, $v_i = 2.78$ on the horizontal trajectory (2). Time advances downward in both spatiotemporal records which display the time evolution during 32 s.

tion occurs in reverse between $v_e = 0.58$ and 0.77.) With further increase of v_i, λ again decreases monotonically while v_d continues to increase. The interface profiles observed at $v_i = 1.61$ and 2.78, despite their very different shapes, are both uniform traveling cell states as seen in the spatiotemporal plots of Fig. 9.

In Fig. 10, the wavelength λ is plotted against v_i for the horizontal trajectories (1; $v_e = 0$) and (2; $v_e = 0.10$). The figure shows the jump in λ for $v_e = 0.1$ near $v_i = 1.5$, while for $v_e = 0$, λ decreases monotonically.

The wavelengths and drift speeds of the S cells and L cells measured with higher resolution for three trajectories $v_e = 0.10$, 0.25, and 0.35 are shown in Figs. 11 and 12, respectively. At $v_e = 0.10$, the wavelength of the S cells decreases rapidly with increasing v_i; for larger v_e the decrease is slower.

The S cells have relatively well-defined wavelengths (particularly at large v_e) but considerable scatter in their drift speed which shows little or no dependence on v_i. This scatter is probably due to slight imperfections in the outer cylinder which induce a periodic modulation in v_d of about 20% as shown in Fig. 13.

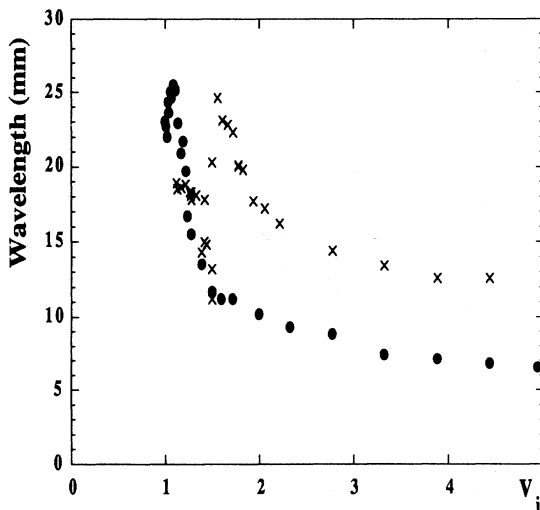In contrast to the S cells, it is evident in Fig. 11 that

FIG. 10. Wavelength λ vs v_i for $v_e = 0$ (●) and $v_e = 0.1$ (×). Spacing is $b_0 = 0.7$ mm.

close to the S-L bifurcation the L cells have considerable dispersion in wavelength, while their drift speeds are remarkably constant as seen in Fig. 12. Beyond the S-L bifurcation, the wavelength of the L cells decreases while their drift speed increases monotonically. Beyond v_{c3}, no further bifurcations were observed. From these experiments, the partial state diagram shown in Fig. 14 was constructed, showing the locations of v_{c1}, v_{c2}, and v_{c3} for v_e in the range 0.1 to 0.5.

Characterization of the bifurcations

Although the primary planar-cellular bifurcation at v_{c1} is homogeneous, the second stationary cell-traveling cell bifurcation at v_{c2} and the third S cell-L cell bifurcation at v_{c3} both occur through relatively complicated inhomogeneous mechanisms. The stationary cell-traveling cell bifurcation at v_{c2} can occur in two ways. For $v_e > 0.25$, the first moving cells to appear are usually solitons, as shown in Fig. 15. One or more such highly asymmetric cells moves rapidly across the interface, destroying the cells they cross, which are then reconstituted behind them. The passage of these solitons does not produce any obvious change in the dominant pattern, although the distribution of cell sizes before and after the passage of solitons has not been investigated quantitatively. However, it has been shown previously that the phase of the underlying stationary structure is not affected by the passage of solitons [3]. Presumably, this is because of a memory effect introduced by the wetting film on the rotating cylinders. For $v_e = 0.1$, the appearance of traveling cells occurs when a group of stationary cells tilts and begins to drift as seen in Fig. 16, without destroying any of the stationary cells.

For $v_e > 0.1$ and between v_{c2} and v_{c3}, fast cells (solitons or groups of L cells) can appear in addition to the dominant S cells. Near v_{c3}, L cells appear through the destabilization of existing S cells. This destabilizing transition is reversible and may occur periodically at the period of the outer cylinder rotation, as shown in Fig. 17. Since the number of cells is conserved, the boundary between the small and large cells drifts at a speed V_B, given by

$$V_B = \frac{V_L \lambda_S - V_S \lambda_L}{\lambda_L - \lambda_S} ,$$
(2.1)

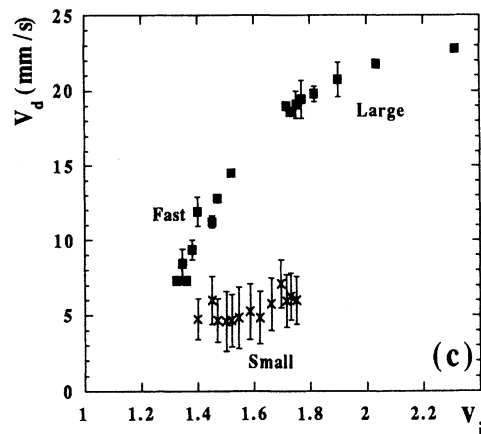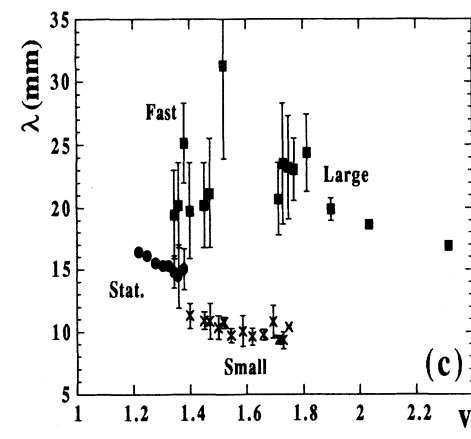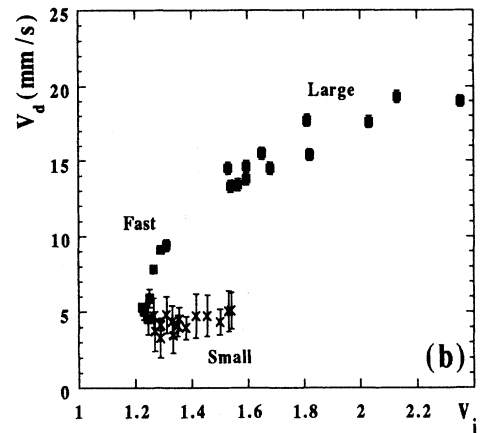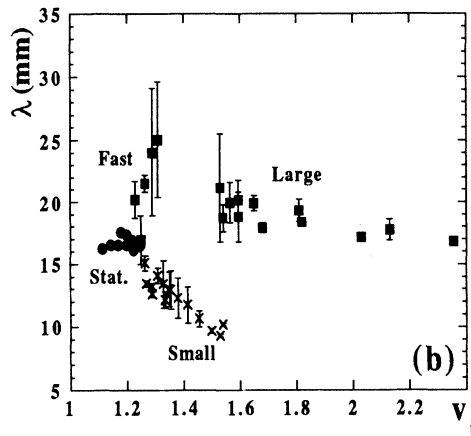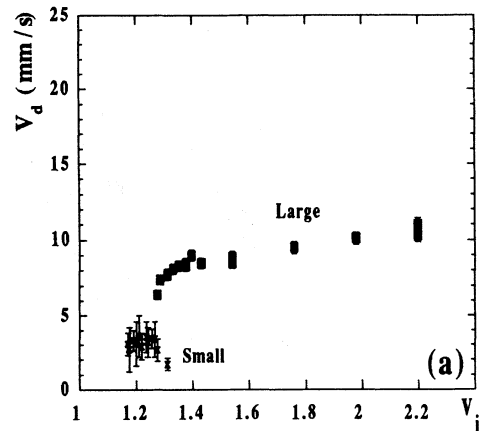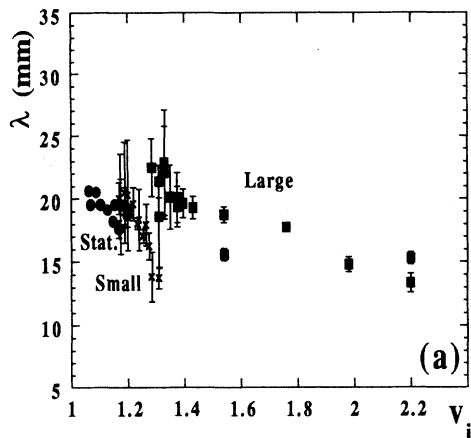At larger values of v_e, L cells frequently appear first at

FIG. 11. Wavelength λ vs v_i for $v_e = 0.10$ (a), 0.25 (b), and 0.35 (c). "Stat" (●) refers to stationary cells, "Small" (×) to small cells, "Large" (■) to large cells, and "Fast" (■) to either solitons or isolated L cells occurring in the S-cell region between v_{c2} and v_{c3}. Error bars represent the extreme of values observed during 100 s.

FIG. 12. Drift speed v_d vs v_i for $v_e = 0.10$ (a), 0.25 (b), and 0.35 (c). "Small" (×) refers to small cells, "Large" (■) to large cells, and "Fast" (■) to either solitons or isolated L cells occurring in the S-cell region between v_{c2} and v_{c3}. Error bars represent the extreme of values observed during 100 s.
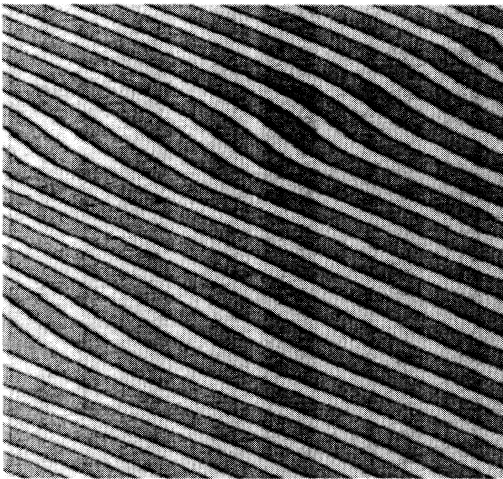
FIG. 13. Spatiotemporal record at $v_e = 0.35$ and $v_i = 1.64$, illustrating the fluctuation in v_d for S cells.

sources, and convert to S cells near a sink as seen in Fig. 18. Such sources and sinks appear and disappear frequently, and a domain of traveling cells anywhere along the front is equally likely to be found moving to the right or left. The large rapidly moving cells on the right of Fig. 18 transform continuously into narrow slowly moving cells at a boundary which can remain essentially fixed for long times if source and sink are motionless. In general, as these defects move, such boundaries are not fixed. When the boundary is fixed, conservation of cells results in the ratio v_d / λ being constant. These patterns of coexisting large and small cells persist for long times, eventually disappearing but reappearing again for as long as we observed them (maximum of 2.5 h).

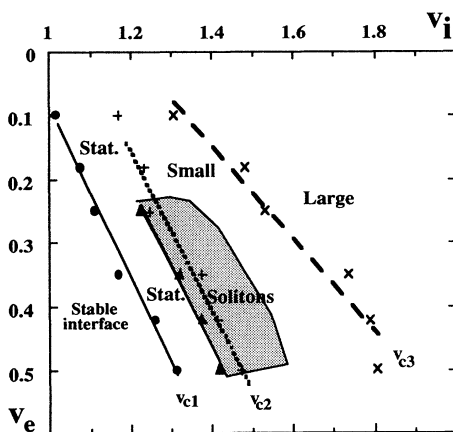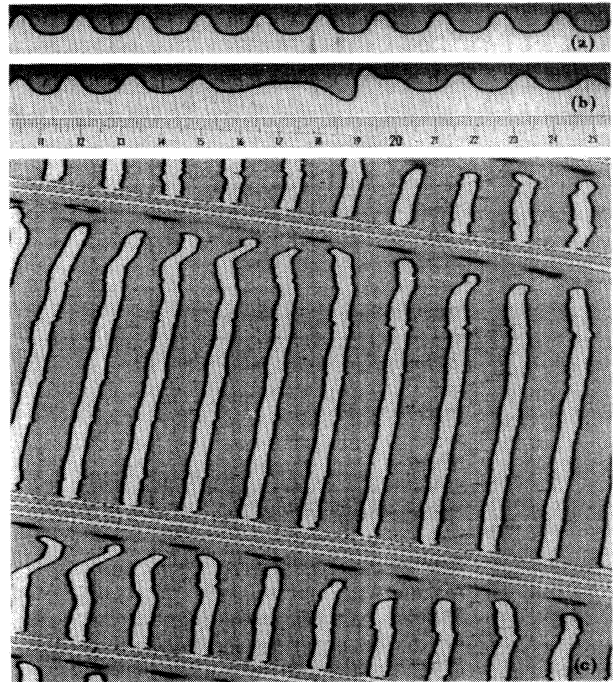One interpretation of these mixed-cell regimes is that

FIG. 15. Interface images before (a) and during (b) the passage from left to right of a solitary traveling cell (soliton). (c) Spatiotemporal record spanning 128 s, showing the passage of three groups of two or three solitons.

in this region of the state diagram the system has two dynamical states which are almost equally stable, and it is unable to select one or the other definitively. Competition between different stable nonequilibrium states in convection experiments, possibly related to the mixed states we have observed here, have been described by Kolodner [16] and by Bensimon et al. [17].

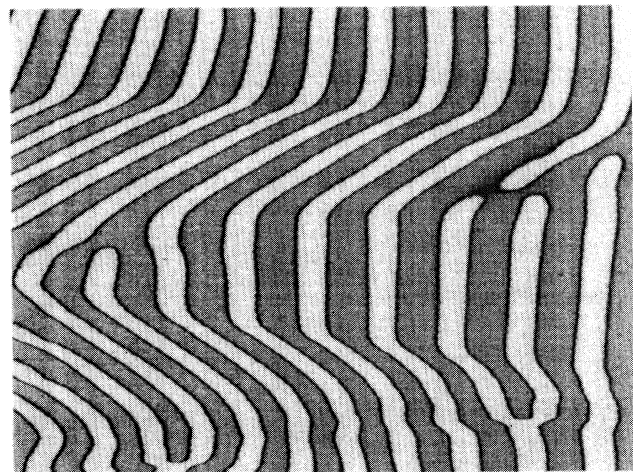As v_i is further increased, these mixed states disappear

FIG. 14. Partial state diagram (zoom of Fig. 3) for the region $v_e = 0.1$ to 0.5 indicating the three bifurcation lines at v_{c1} ($\bullet$), v_{c2} ($+$), and v_{c3} ($\times$) (lines are best linear fit of the data). The points ($\blacktriangle$) and crosshatched area indicate the region in which groups of solitons like those shown in Fig. 15 are observed. v_{c2} and v_{c3} indicate the value of v_i at which the first or last S cells are observed.

FIG. 16. 90 sec spatiotemporal record with $v_e = 0.10$ and $v_i = 1.20$ illustrating the spontaneous reversible tilt bifurcations observed near v_{c2}.
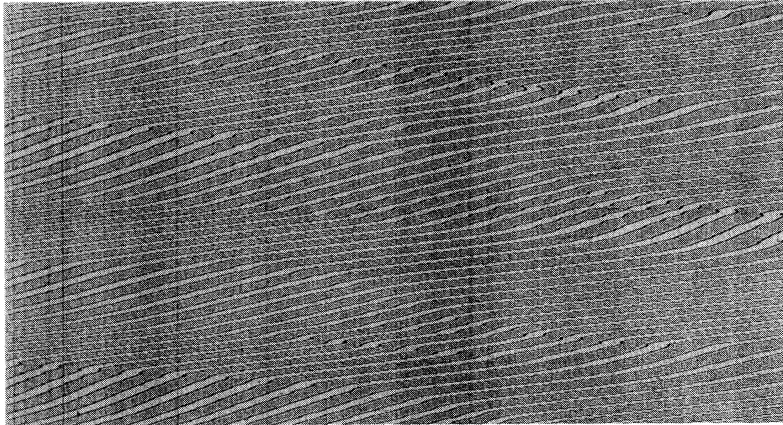
FIG. 17. 162-s spatiotemporal record with $v_e = 0.10$ and $v_i = 1.28$ illustrating spontaneous periodic L-S transitions observed close to v_{c3}, synchronous with the outer cylinder rotation.

and the observed L-cell interface again has a well-defined wavelength and drift speed. Finally, we note two unresolved aspects of the bifurcation sequence requiring further study. First, as Figs. 11 and 12 demonstrate, the S-L bifurcation at v_{c3} occurs with pronounced discontinuities in both wavelength and drift speed. The data are consistent with wavelength doubling, although the large fluctuations close to v_{c3} prevent establishing this ratio with precision. Nevertheless, we tentatively identify the bifurcation at v_{c3} as a spatial period-doubling bifurcation. Second, there are occasional L cells and solitons observed in the S-cell regime between v_{c2} and v_{c3}. We have included them in the drift speed plots in Fig. 12 as "fast" [18].
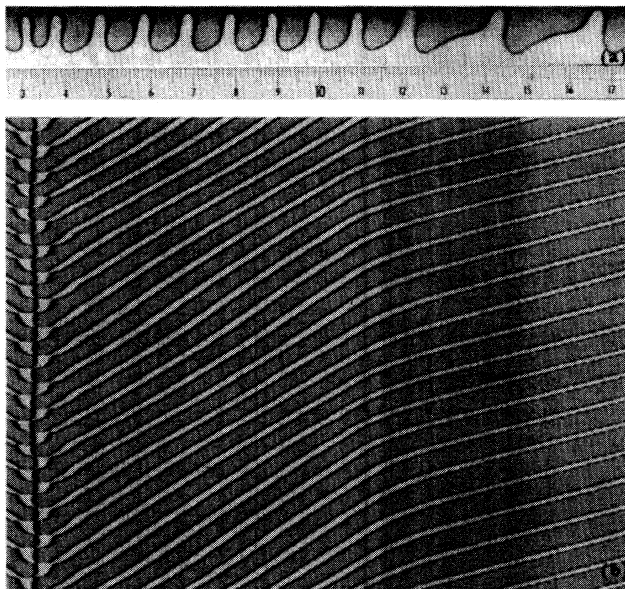

FIG. 18. Coexisting large and small cells at $v_e = 0.25$, $v_i = 1.78$ separated by a stationary front. Interface profile (a); 32-s spatiotemporal record (b). The stationary front is pinned by the sink visible at the left.

III. ANALYSIS

The experiments described in the preceding section have established that in DVF with counter-rotating cylinders with the velocity of the external cylinder v_e fixed, increasing the velocity of the inner cylinder v_i from zero results in three successive bifurcations: a primary bifurcation at v_{c1} from the planar front to a stationary cellular front, then at v_{c2} a tilt bifurcation to traveling tilted cells, and finally at v_{c3} a spatial period-doubling bifurcation (with various transient or mixed regimes observed near the bifurcation thresholds). In this section we consider possible explanations for this bifurcation sequence.

The hydrodynamics and linear stability analysis of directional viscous fingering was discussed by Hakim et al. [1] for the cylinder-plane geometry, and was recently extended to the corotating two-cylinder geometry by Michalland [6]. The theory closely resembles that of the classic Saffman-Taylor problem [19,20], with the addition of a stabilizing term due to the nonuniformity of the distance between the two boundaries. A brief description of the linear stability analysis is given in the Appendix.

A plot of the resulting marginal stability curve for our system with $b_0 = 0.7$ mm and $v_e = 0$ is shown in Fig. 19. We have also included the data of Fig. 5(b) in the figure. Although the mechanism of wavelength selection above the threshold is unknown, Fig. 19 indicates that the selected wavelength lies in the large-k domain of the marginal stability curve (also see Refs. [1] and [6]).

The linear stability analysis results in solutions of the equation

$$\frac{d\xi_k(t)}{dt} = \mu_k \xi_k(t) \qquad (3.1)$$

for $\xi(x,t) = y(x,t) - \langle y(x,t) \rangle$, the deviation of the front position $y(x,t)$ from its mean position $\langle y(x,t) \rangle$. The values of V_i for each k at which μ_k passes through zero define the marginal stability curve. In order to extend the analysis to the nonlinear region inside the curve, higher-order terms must be included. However, a nonlinear hydrodynamic analysis for DVF, which is required to describe the evolution of the interface beyond threshold, does not yet exist.

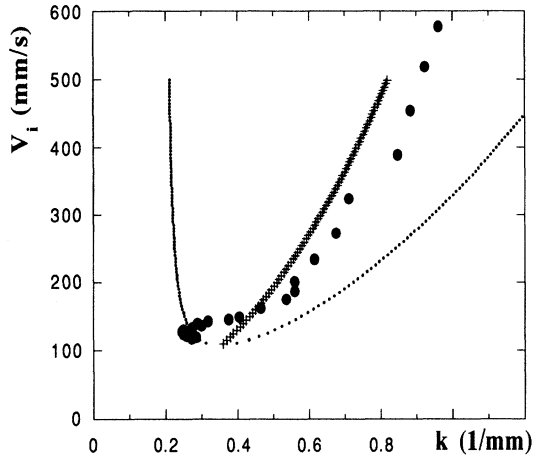An alternative approach to the nonlinear regime, wide-

FIG. 19. Computed marginal stability curve for $b_0 = 0.7$ mm (.), and most unstable mode (+) superimposed with experimentally selected wave number (●) of Fig. 5(b) for $V_e = 0$.

ly used to describe front instabilities, is the phenomenological amplitude (or time-dependent Landau) equation for $\xi(x,t)$. The simplest phenomenological amplitude equation, for a single Fourier component $\xi_k(t)$, is

$$\frac{d\xi_k(t)}{dt} = \mu_k \xi_k(t) - a_3 \xi_k^3(t) + \text{(higher-order terms)} ,$$

(3.2)

where k is taken to be the most unstable wave vector corresponding to the minimum of the marginal stability curve at $V = V_c$, $k = k_c$ (point C in Fig. 20). If $a_3 > 0$, a supercritical (normal) bifurcation occurs when μ_k changes sign at $V = V_c$, and ξ_k subsequently increases with $\mu_k^{1/2}$. Equation (3.2) can only be valid very close to V_c; however, since once ξ_k becomes large enough for
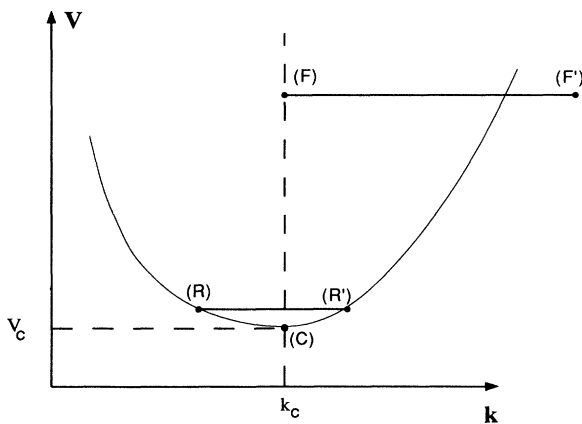

FIG. 20. Schematic marginal stability curve illustrating the initial instability point (C) at (k_c, V_c). Points (F) and (F') represent the k and $2k$ modes in the tilt bifurcation scenario of Fauve, Douady, and Thual [27]. Points (R) and (R') are the k and $2k$ modes at the codimension-2 point.

nonlinear terms to intervene, these terms will also result in mixing of different Fourier components. Equation (3.2) can be generalized either by allowing ξ_k to be a slowly varying function of x and including spatial derivatives in the amplitude equation (time-dependent Ginzburg-Landau equation), or by including more than one Fourier component in $\xi(x,t)$.

Malomed and Tribelsky [21] analyzed several nonlinear amplitude equations, using trial solutions of the form $\xi(x,t) = A_1(t)\sin kx + A_2(t)\cos 2kx + \cdots$. They discovered that following the initial bifurcation to the stationary pattern $\xi(x,t) = A_1 \sin kx$, there would be an increasingly important admixture of A_2 and a secondary bifurcation to a state with cells traveling with a constant velocity. The secondary bifurcation was shown to arise from the fact that μ_2, the linear gain coefficient of the $\cos 2kx$ term, which is negative, increases toward zero as the control parameter increases.

Several authors have analyzed the most general amplitude equations, including all terms through third order allowed by symmetry, for the two-mode trial function

$$\xi(x,t) = z_1 e^{ikx} + z_2 e^{i2kx} + \text{c.c.}$$

(3.3)

The coupled amplitude equations are

$$\frac{dz_1}{dt} = \mu_1 z_1 + c_1 z_1^* z_2 + a_1 z_1 |z_1|^2 + b_1 z_1 |z_2|^2 ,$$

$$\frac{dz_2}{dt} = \mu_2 z_2 + c_2 z_1^2 + b_2 z_2 |z_1|^2 + a_2 z_2 |z_2|^2 .$$

(3.4)

Letting $z_1 = \rho e^{i\phi}$, $z_2 = \sigma e^{i\theta}$ (with ρ and σ real), and $\Sigma = 2\phi - \theta$, Eqs. (3.4) reduce to

$$\frac{d\rho}{dt} = \mu_1 \rho + a_1 \rho^3 + b_1 \sigma^2 \rho + c_1 \sigma \rho \cos\Sigma ,$$

(3.5a)

$$\frac{d\sigma}{dt} = \mu_2 \sigma + b_2 \rho^2 \sigma + a_2 \sigma^3 + c_2 \rho^2 \cos\Sigma ,$$

(3.5b)

$$\frac{d\Sigma}{dt} = -(c_2 \rho^2/\sigma + 2c_1 \sigma)\sin\Sigma ,$$

(3.5c)

$$\frac{d\phi}{dt} = -c_1 \sigma \sin\Sigma .$$

(3.5d)

Jones and Proctor [22,23] used these equations to investigate traveling waves in Bénard convection. Levine, Rappel, and Riecke [24–26] used them to explain the parity-breaking tilt bifurcation observed in the directional solidification experiments of Simon and co-workers [9,10]. Rappel and Riecke [26] also solved the basic solidification equations numerically and compared the results with the predictions of the amplitude equations.

Equations (3.5) have three different types of steady-state solutions [26]: pure $2k$ modes (S_2), stationary mixed k-$2k$ modes (S_+, S_-), and traveling cell modes (T). Figure 21, based on the results of Jones and Proctor [22], shows a schematic (partial) bifurcation diagram for Eqs. (3.4) in the space of the two linear gain coefficients μ_1 and μ_2. (The shape of the boundaries depends on the choice of the coefficients.)

Fauve, Douady, and Thual [27] considered a scenario in which the initial instability occurs for $k = k_c$ at point (C) in Fig. 20. As V increases, and μ_1 becomes more pos-
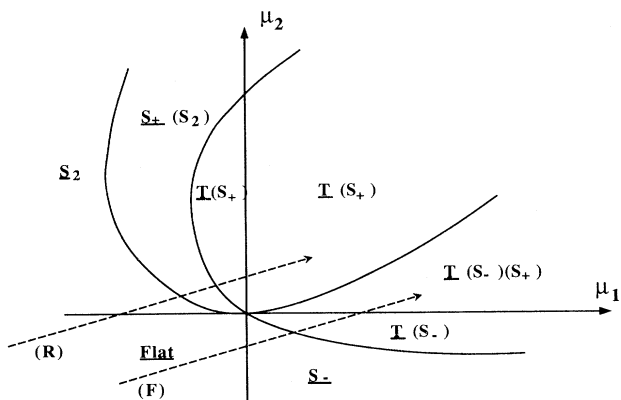
FIG. 21. Schematic bifurcation diagram from Eqs. (3.4) based on Ref. [22]. S_2: pure $2k$ mode. S_+,S_-: stationary mixed k-$2k$ modes. T: traveling cell mode. Modes shown in parentheses are allowed but unstable. The dashed lines R and F are the trajectories discussed in the text.

itive, the fundamental amplitude ρ of the stationary pattern increases, while the harmonic amplitude σ increases as ρ^2. The stationary pattern is eventually destabilized and undergoes a secondary supercritical bifurcation to a tilted traveling-wave state (drift bifurcation) when μ_2 (assumed negative) increases and becomes sufficiently close to zero, as first noted by Malomed and Tribelsky [21]. Above the threshold the pattern consists of tilted waves which drift with a constant speed v_d.

In Fig. 21, this trajectory is represented by the line F. As V increases to the point where μ_1 becomes positive, the flat interface bifurcates to the stationary mixed mode S_-; on crossing the lower curved boundary, the S_- mode becomes unstable and the second bifurcation occurs to the traveling cell mode T.

For directional viscous fingering with one cylinder fixed, the secondary bifurcation to a steady-state traveling cell mode does not occur. As discussed above, increasing the inner cylinder rotation velocity to 50 times threshold still produces stationary symmetric cells. And as shown in Fig. 6, for $v_e=0$ the amplitude ratio of the second harmonic to the fundamental decreases with increasing v_i rather than increasing. As v_i increases, the dynamically selected wavelength decreases, remaining close to the boundary of the marginal stability curve, as shown in Fig. 19, so that the $2k$ mode always remains far outside of the marginal stability curve, in the stable region.

If v_i is increased abruptly, however, starting from a point just above threshold, then before the wavelength has time to adjust the system can move to a point F (Fig. 20) close to the midline of the stability curve so that μ_2 can be much closer to zero. A tilt bifurcation can then occur as a transient, until k has time to readjust. This scenario, which was discussed by Fauve, Douady, and Thual [27], presumably explains the observed transient drifting states observed with $v_e=0$ [5].

Rappel and Riecke [26] (also see [23–25]) considered bifurcation sequences that can occur in the vicinity of the

codimension-2 point (R-R' in Fig. 20) where both the k and $2k$ modes become linearly unstable simultaneously. Transitions between the three solutions of Eqs. (3.5) can occur in various ways, depending on the values of the coefficients. In particular, in our experiments, if the initial instability at (C) in Fig. 20 is designated as $2k$, then with increasing v_i the system approaches point (R') inside the curve and the k mode at (R) approaches instability. This corresponds to the trajectory R in Fig. 21 where the flat interface bifurcates to the pure $2k$ mode (S_2) when μ_2 changes sign, followed by secondary bifurcations to the mixed state S_+ and then to the traveling cell state T. This approach, in contrast to that of Fauve, Douady, and Thual predicts first a spatial period-doubling bifurcation and then a tilt bifurcation.

However, neither the scenario of Fauve (F) nor that of Rappel and Riecke (R) can explain the bifurcation sequence observed in our experiments, because the wavelength of the pattern is always determined by the smallest wave vector present. Thus, in the scenario F, the wavelength of the pattern with fundamental k is always $\lambda=2\pi/k$, and is not changed by the admixture of the $2k$ component. The tilt bifurcation occurs with no change in wavelength (as we observed), but no period-doubling bifurcation is possible.

In the scenario R, it is possible for the initial planar-cellular bifurcation to produce a pure $2k$ state S_2 with wavelength $\lambda=\pi/k$ at point (R) which can then bifurcate to the stationary mixed state S_+ and then to the traveling-wave state T. But the admixture of the k mode will cause the wavelength to double to $\lambda=2\pi/k$, so that a tilt bifurcation without change in wavelength cannot occur.

We therefore conclude that k-$2k$ models cannot explain the bifurcation sequence observed in the DVF experiments. We propose that the simplest model that can possibly explain the sequence of three bifurcations will require three modes rather than two, i.e.,

$$\xi(x,t)=z_1e^{ikx}+z_2e^{i2kx}+z_4e^{i4kx}+\text{c.c.} \tag{3.6}$$

With this trial function, the initial mode would be z_2, with an increasing admixture of z_4 that would eventually lead to a tilt bifurcation without change in wavelength (as in the scenario F), followed by another bifurcation to a state containing some z_1, which would then produce spatial period doubling.

The amplitude equations for this case, including all terms through third order allowed by translational invariance, are

$$\frac{dz_1}{dt}=\mu_1z_1+c_1z_1^*z_2+a_1z_1|z_1|^2+b_1z_1|z_2|^2$$
$$+d_1z_1|z_4|^2+e_1z_1^*z_2^*z_4$$

$$\frac{dz_2}{dt}=\mu_2z_2+c_2z_1^2+e_2z_4z_2^*+b_2z_2|z_1|^2$$
$$+a_2z_2|z_2|^2+d_2z_2|z_4|^2+f_4z_4z_1^{*2}$$

$$\frac{dz_4}{dt}=\mu_4z_4+c_4z_2^2+b_4z_4|z_1|^2+a_4z_4|z_2|^2$$
$$+d_4z_4|z_4|^2+e_4z_1^2z_2 \tag{3.7}$$

An analysis of these amplitude equations and of the possible bifurcation sequences they allow has not yet been undertaken.

Note added in proof. Due to a small shift in the oil viscosity, the dimensionless parameter v_i of Figs. 8 and 9 are are overestimated by a factor of 1.16. We thank P. Kolodner for pointing this out to us.

ACKNOWLEDGMENTS

APPENDIX: LINEAR STABILITY ANALYSIS

We will now present briefly a linear analysis of DVF. More details can be found in Refs. [1] and [6]. The flow of a single fluid located between eccentric rotating cylinders of similar radius can be solved in the lubrication approximation. The analysis for any radius with inertial corrections can be found in Ballal and Rivlin [28]. For our purpose it is sufficient to consider the narrow region as parabolic with a thickness $b(x)$ given by

$$b(x) = b_0 + \frac{x^2}{2R} \quad \text{with} \quad \frac{1}{R} = \frac{1}{R_i} - \frac{1}{R_e} ,$$

where R is the equivalent radius of the inner (R_i) and external (R_e) cylinders and x is an orthoradial abscissa. Velocity being mainly orthoradial, it is a superposition of a planar Couette profile and of a parabolic Poiseuille profile due to the pressure gradient. (The pressure is found to obey a diffusionlike equation.) Integrating this pressure equation, the flow rate between the cylinders is found to be

$$Q = \frac{2b_0}{3}(V_i + V_e) .$$

In the case of two fluids in the system, surface-tension corrections are found to be unimportant in the determination of Q [1].

It is more difficult to determine the position of the meniscus. In a two-dimensional model and with stationary experimental conditions, oil conservation gives the relation $Q = Q_i + Q_e$ between the total flux Q and the two fluxes carried by the coating films on the two rotating cylinders. This coating flux (positive or negative) is given by the product of the boundary velocity by the thickness of the film far from the meniscus: $Q_i = V_i t_i$ and $Q_e = V_e t_e$. For $V_e = 0$, $Q_e = 0$ so the conservation of oil gives a constant value for t_i. This conclusion is contradicted by experiments as t_i is observed to increase with the surface velocity V_i. We believe that this discrepancy is due to a three-dimensional effect with a transverse oil flow coming from the ends, and we will not take this effect into account here.

Until now we have no data for the global evolution of the position of the meniscus with the two velocities V_i and V_0. Therefore, for the following analysis, we will suppose that one cylinder is at rest (e.g., $V_e = 0$) and that the position of the initially planar meniscus is given by a dimensional relation, as in the problem of the coated film drawn by an infinite plane: $t = F(\text{Ca})b_m$, where b_m is the thickness of the gap where the meniscus is located, $\text{Ca} = \eta V / T$ is the capillary number, and F is a function taken from a fit of our experiment and the compilation by Ruschák [8] of other experiments [29]. We take as a best fit in our range $0 < \text{Ca} < 2$:

$$F(\text{Ca}) = 0.24[1 - \exp(-8.6\text{Ca}^{2/3})] .$$

This relation gives the location of the meniscus for $V_e = 0$ by

$$b_m = \frac{2b_0}{3F(\text{Ca})} .$$

Once the locus of the meniscus is determined, the linear analysis follows. For any Fourier mode, the equations of the pressure field, velocity field, and conservation of fluid at the moving interface are linearized. Assuming in order to be analytic that

$$\frac{1}{b}\left[\frac{\partial b}{\partial x}\right]$$

is constant along the profile (which is not really the case as it requires locally an exponential thickness profile), the growth rate μ of the mode of wave number k is found to be

$$\mu(k,\text{Ca}) = \frac{TM(k)}{12\eta[1-F(\text{Ca})]}\left[\text{Ca}\left(6 - 8\frac{b_0}{b_m} - 8\frac{b_0 G}{b_m^2 M(k)}\right) - 2G - b_m^2 k^2\right] , \quad (\text{A1})$$

where

$$G = \left[\frac{\partial b}{\partial x}\right]_{x_m}$$

at the meniscus location, and

$$M(k) = \frac{1}{H}[(1 + H^2 k^2)^{1/2} - 1]$$

with

$$H = \frac{2b_m}{3G} .$$

It is worth noting that at constant capillary number Ca, the quantities b_m, G, and H are constant and so the sign of the growth rate is given by the sign of the right-hand part of Eq. (A1). It is now simple to construct the marginal stability curve by solving $\mu(k,\text{Ca}) = 0$ (Fig. 19). For any Ca the most unstable mode k_c is given by $\partial\mu/\partial k = 0$. We found that

$$k_c = (\sqrt{S-1} + \sqrt{S+1})\frac{G}{b_m}$$

$$\text{with} \quad S = \frac{2\text{Ca}}{G^2}[1 - 2F(\text{Ca})] - \frac{2}{3G} .$$

*Permanent address: Department of Physics, City College, CUNY, New York, NY 10031.

[1] V. Hakim, M. Rabaud, H. Thomé, and Y. Couder, in *New Trends in Non-linear Dynamics and Pattern Forming Phenomena: The Geometry of Non equilibrium*, edited by P. Coullet and P. Huerre (Plenum, New York, 1990), p. 327.

[2] M. Rabaud and V. Hakim, in *Instabilities and Non equilibrium Structures III*, edited by E. Tirapegui and W. Zeller (Kluwer Academic, Dordrecht, 1991), p. 217.

[3] Y. Couder, S. Michalland, M. Rabaud, and H. Thomé, in *Non-linear Evolution of Spatio-Temporal Structures in Dissipative Continuous Systems*, edited by F. H. Busse and L. Kramer (Plenum, New York, 1990), p. 487.

[4] M. Rabaud, S. Michalland, and Y. Couder, Phys. Rev. Lett. 64, 184 (1990).

[5] M. Rabaud, Y. Couder, and S. Michalland, Eur. J. Mech. B 10, S253 (1991).

[6] S. Michalland, Thèse de l'Université Paris VI, 1992 (unpublished).

[7] S. Michalland and M. Rabaud, Physica D 61, 197 (1992).

[8] K. J. Ruschak, Annu. Rev. Fluid Mech. 17, 65 (1985).

[9] A. J. Simon, J. Bechhoefer, and A. Libchaber, Phys. Rev. Lett. 61, 2574 (1988).

[10] J-M. Flesselles, A. J. Simon, and A. J. Libchaber, Adv. Phys. 40, 1 (1991).

[11] G. Faivre and J. Mergy, Phys. Rev. A 45, 7320 (1992).

[12] G. Faivre and J. Mergy, Phys. Rev. A 46, 963 (1992).

[13] G. Faivre, S. De Cheveigne, C. Guthmann, and P. Kurowski, Europhys. Lett. 9, 779 (1989).

[14] We considered two possible explanations for the fact that trajectory (1) ($V_e = 0$) does not produce a tilt bifurcation. First, as noted previously as V_i is increased beyond V_c, the (unknown) dynamical selection mechanism causes the selected wavelength λ of the stationary cellular pattern to decrease rapidly, with k remaining close to the upper boundary of the marginal stability curve. This wavelength selection results in the second harmonic ($2k$) always falling far below the marginal stability curve so that the condition that the second harmonic not be too strongly damped, which is a requirement for the secondary bifurcation, cannot be met. We have observed that the bifurcation from stationary to traveling cells obtained with a vertical trajectory of type A usually leads to a significant increase in λ. A second possible explanation is that if $V_e = 0$, the dry boundary condition imposes an additional major friction force for traveling waves which blocks the stationary cell—traveling cell bifurcation.

[15] This initial increase in wavelength is always observed when the internal cylinder rotates with the external cylinder fixed [6]. We believe that it is caused by gravitational forces on the meniscus.

[16] P. Kolodner, Phys. Rev. Lett. 66, 1165 (1991).

[17] D. Bensimon, P. Kolodner, C. M. Surko, H. Williams, and V. Croquette, J. Fluid Mech. 217, 441 (1990).

[18] Qualitatively, the velocities of the solitons and drift speeds of the isolated L cells seen in Fig. 12 between v_{c2} and v_{c3} follow the same increasing curve as that of the L cells beyond v_{c3}. This observation could suggest that the region between v_{c2} and v_{c3} does not constitute a true stationary regime. Although additional experiments are required to resolve this point, we believe that the most coherent interpretation of the data is the three-bifurcation state diagram shown in Fig. 14.

[19] P. G. Saffman and G. Taylor, Proc. R. Soc. London, Ser. A 245, 312 (1958).

[20] D. Bensimon, L. P. Kadanoff, S. Liang, B. I. Shraiman, and C. Tang, Rev. Mod. Phys. 58, 977 (1986).

[21] M. Malomed and M. I. Tribelsky, Physica 14D, 67 (1984).

[22] C. A. Jones and M. R. E. Proctor, Phys. Lett. A 121, 224 (1987).

[23] M. R. E. Proctor and C. A. Jones, J. Fluid Mech. 188, 301 (1988).

[24] H. Levine, W-J. Rappel, and H. Riecke, Phys. Rev. A 43, 1122 (1991).

[25] H. Levine and W-J. Rappel, Phys. Rev. A 42, 7475 (1990).

[26] W-J. Rappel and H. Riecke, Phys. Rev. A 45, 846 (1992).

[27] S. Fauve, S. Douady, and O. Thual, J. Phys. (Paris) II 1, 311 (1991).

[28] B. Y. Ballal and R. S. Rivlin, Arch. Rat. Mech. Anal. 62, 237 (1976).

[29] H. Benkreira, M. F. Edwards, and W. L. Wilkinson, Chem. Eng. Sci. 36, 429 (1981).
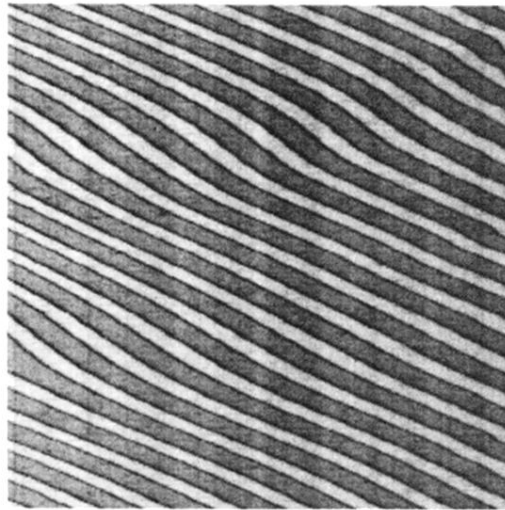
FIG. 13. Spatiotemporal record at $v_e = 0.35$ and $v_i = 1.64$, illustrating the fluctuation in v_d for S cells.
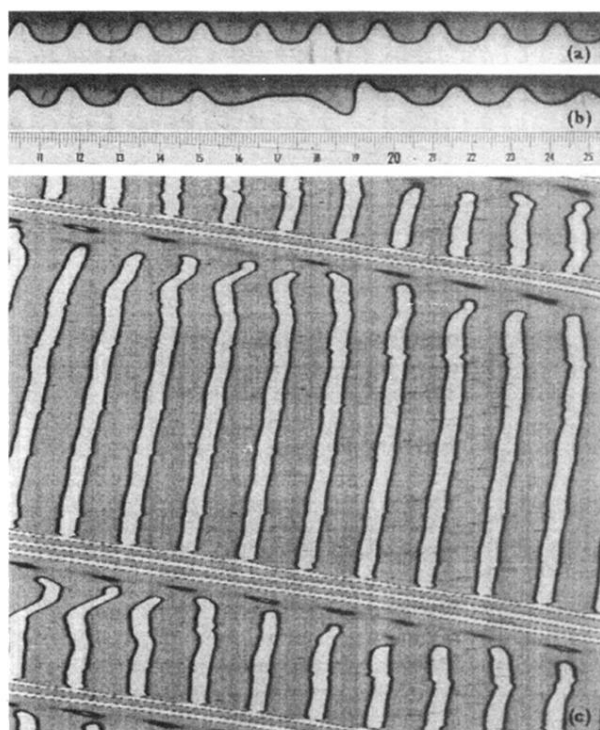
FIG. 15. Interface images before (a) and during (b) the passage from left to right of a solitary traveling cell (soliton). (c) Spatiotemporal record spanning 128 s, showing the passage of three groups of two or three solitons.
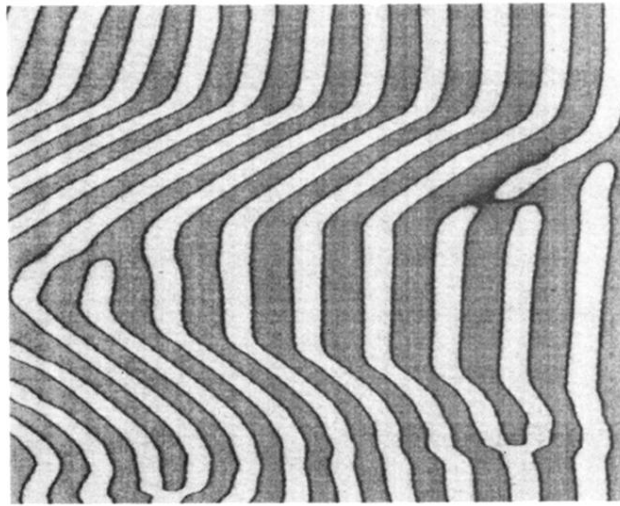
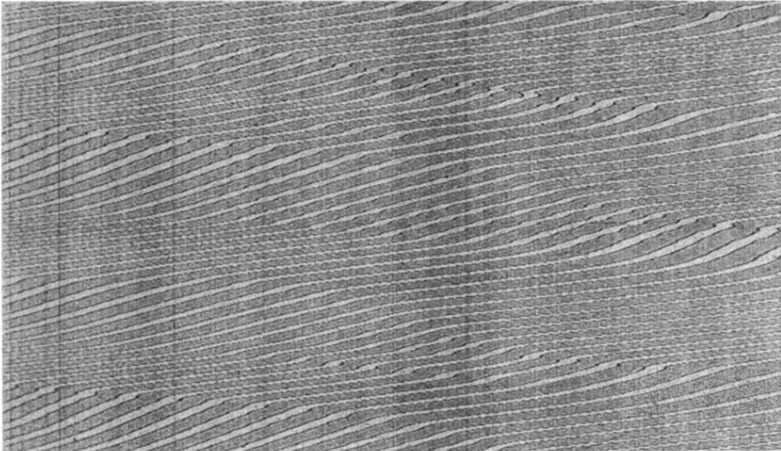FIG. 16. 90 sec spatiotemporal record with $v_e = 0.10$ and $v_i = 1.20$ illustrating the spontaneous reversible tilt bifurcations observed near v_{c2}.

FIG. 17. 162-s spatiotemporal record with $v_e = 0.10$ and $v_i = 1.28$ illustrating spontaneous periodic L-S transitions observed close to v_{c3}, synchronous with the outer cylinder rotation.
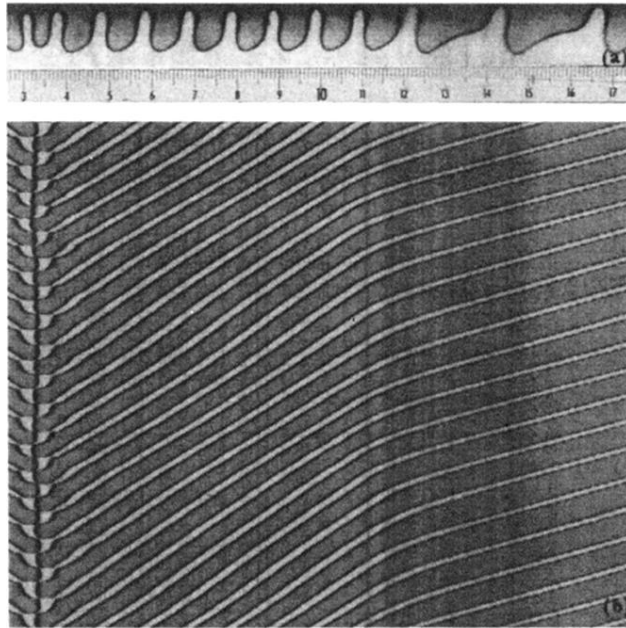
FIG. 18. Coexisting large and small cells at $v_e = 0.25$, $v_i = 1.78$ separated by a stationary front. Interface profile (a); 32-s spatiotemporal record (b). The stationary front is pinned by the sink visible at the left.
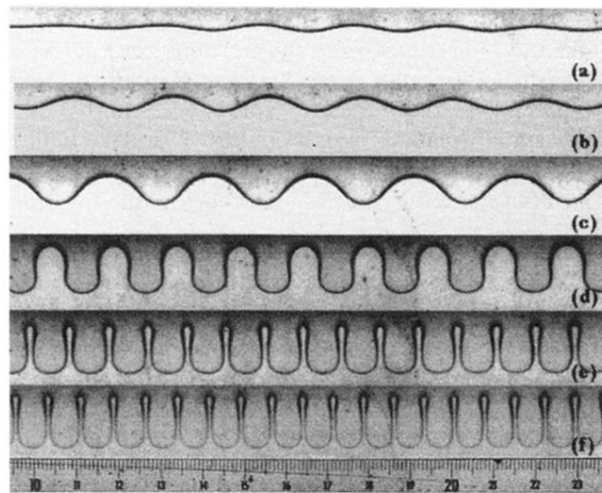
FIG. 4. Observed interface profiles for trajectory (1) ($v_e = 0$) for spacing $b_0 = 0.7$ mm, with (top to bottom) $v_i = 1.00$ (a), 1.02 (b), 1.07 (c), 1.28 (d), 2.32 (e), and 3.33 (f). In these images, the air is above the oil. The scale is in centimeters.
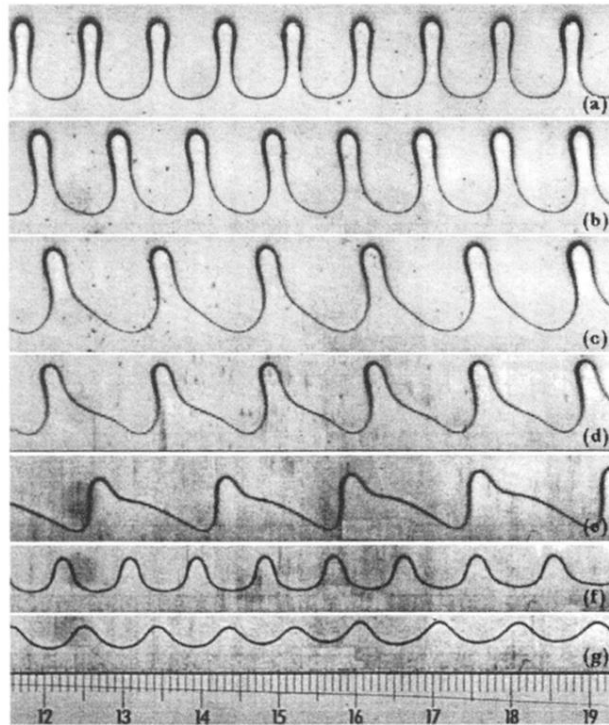
FIG. 7. Interface profiles for $v_i = 2.1$ (trajectory $A1$) with $v_e = 0$ (a), 0.05 (b), 0.1 (c), 0.19 (d), 0.58 (e), 0.77 (f), and 0.96 (g). Spacing is $b_0 = 0.5$ mm.
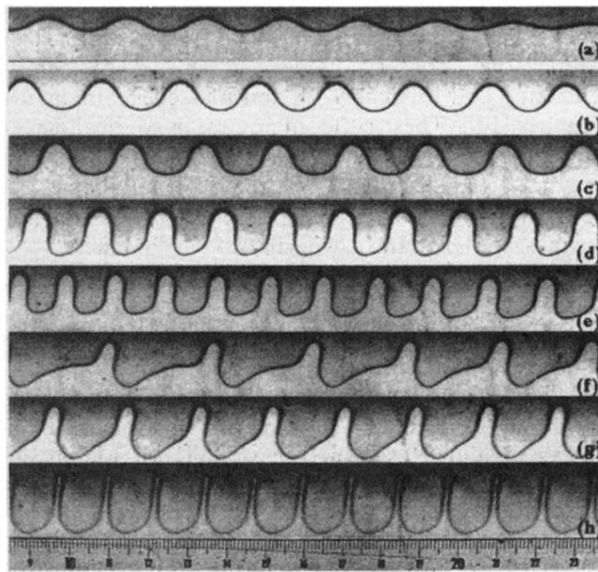
FIG. 8. Interface profiles for the horizontal trajectory (2) $v_e = 0.10$ and spacing $b_0 = 0.7$ mm, $v_i = 1.17$ (a), 1.26 (b), 1.33 (c), 1.39 (d), 1.50 (e), 1.56 (f), 1.94 (g), and 4.44 (h). The tilt bifurcation occurred near $v_i = v_{c2} = 1.38$, between (c) and (d). The S-L bifurcation occurred near $v_i = v_{c3} = 1.52$, between (e) and (f).
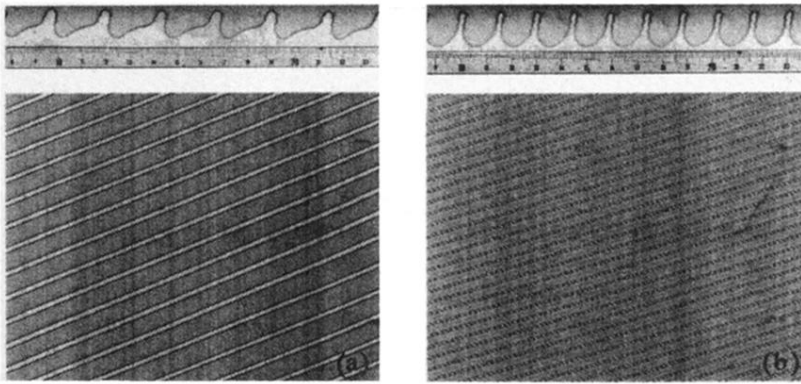
FIG. 9. Images (top) and single video-line spatiotemporal records (bottom) for (a) $v_e = 0.1$, $v_i = 1.61$, and (b) $v_e = 0.1$, $v_i = 2.78$ on the horizontal trajectory (2). Time advances downward in both spatiotemporal records which display the time evolution during 32 s.